Automation in Construction 174 (2025) 106090

Contents lists available at ScienceDirect

Automation in Construction

journal homepage: www.elsevier.com/locate/autcon

Dynamic robotic bricklaying force-position control considering mortar dynamics for enhanced consistency

Yi Zhou [a], Bowen Huang [a], Boge Dong [a], Yi Wen [a], Molong Duan [a,b,*]

[a] Department of Mechanical and Aerospace Engineering, The Hong Kong University of Science and Technology, Hong Kong, SAR, China
[b] HKUST Shenzhen-Hong Kong Collaborative Innovation Research Institute, Futian, Shenzhen, China

ARTICLE INFO

Keywords:
Force-position control
Robotic bricklaying
Construction robot
Viscoelastic mortar dynamics
Bond strength

ABSTRACT

With growing construction automation needs and aging workforce, robotic bricklaying technologies offer promising solutions by replacing labor-intensive manual wall construction. Despite advances in mechatronics, trajectory generation, and adhesive bonding, bricklaying process consistency still remains a major issue, challenged by nonlinear mortar dynamics, variable thickness, and lack of force-position control. This paper enhances consistency by adjusting the robot trajectory to achieve the desirable maximum contact force and brick placement accuracy. The feedforward bricklaying trajectory is generated by solving an optimal control problem with unspecified terminal time to approach the desirable maximum force while maintaining placement accuracy, considering the identified mortar dynamics. To ensure precise positioning and robust desired maximum contact force, robotic bricklaying force-position feedback control is proposed to dynamically control the velocity utilizing real-time force feedback. Simulations and experiments validated the proposed approach, including shear tests, demonstrating enhanced consistency and the relationship between maximum contact force and bond strength.

Nomenclature

t_0	Time when the contact between bricks begins
t_c	Current time
t_e	Time when the desired position x_d is reached
x_0	Robot end-effector position when the contact between bricks begins at the time t_0
x_c	Current robot end-effector position
x_d	Desired robot end-effector position
Δx	Gap distance between the current robot end-effector position x_c and the desired robot end-effector position x_d
x_b	Braking distance
$\widehat{F}_m$	Estimated maximum contact force between bricks
F_d	Desired maximum contact force between bricks
F_c	Current contact force feedback between bricks
F_e	External disturbance force measured by the load cell
F_i	Inertial force of the brick
v_0	Initial velocity of the robot end effector at time t_0
v_c	Current velocity of the robot end effector at time t_c
v_e	Terminal velocity of the robot end effector at time t_e
$v_{\max}$	Maximum compressing velocity in the bricklaying process
v_s	Specified constant velocity in the multi-stage trapezoidal velocity motion profile
$\underline{v}$	Minimum velocity for v_s during the constant velocity movement period in the multi-stage trapezoidal velocity motion profile
$\overline{v}$	Maximum velocity for v_s during the constant velocity movement period in the multi-stage trapezoidal velocity motion profile
v_r	Reshaped velocity generated by the force-positon control
A_m^+	Maximum acceleration
A_m^-	Maximum deceleration
A_r^+	Rated acceleration
A_r^-	Rated deceleration
k_f	Force-regulating coefficient

1. Introduction

The construction sector globally has been adopting new technologies due to rapid urbanization and workforce shortages [1]. Construction

* Corresponding author at: Department of Mechanical and Aerospace Engineering, The Hong Kong University of Science and Technology, Hong Kong, SAR, China.
E-mail address: duan@ust.hk (M. Duan).

https://doi.org/10.1016/j.autcon.2025.106090
Received 3 September 2024; Received in revised form 11 February 2025; Accepted 20 February 2025
Available online 13 March 2025

tasks, especially bricklaying, are time-consuming and labor-intensive with high demands for construction product quality [2,3]. To address these challenges, robotic bricklaying technologies are the most promising technologies for brick wall construction [4]. Representative robotic bricklaying platforms, including the robotic manipulator [5–8], mobile bricklaying robot [1], [9–12], cable-driven bricklaying robot [13], multi-robot bricklaying system [14,15], and large-scale bricklaying system with a telescopic arm [16], have been proposed. Liu et al. [5] proposed an innovative teleoperation robotic bricklaying system that frees workers from using hands and arms. Raković et al. [6] presented a parametric architectural design of bricklaying walls fabricated by an industrial robotic arm. Usmanov et al. [7] designed a functional reduced-scale bricklaying industrial robot capable of technically implementing the complete process of bricklaying. Dörfler et al. [11] described the implementation of a situ bricklaying construction process using a location-aware mobile robot. Helm et al. [12] employed an existing mobile industrial robot, considering handling tolerances, man-machine interactions, and the mobility of the fabrication unit. Wu et al. [13] proposed a cable-driven brick structure building system with a buildable workspace. Ambrosino et al. [14] proposed a multi-robot bricklaying system with a crane and a lightweight rigid robot to operate the large and heavy bricks. Piškorec et al. [15] introduced an automated multi-robotic system for dry brick stacking at a large scale including custom-made robotic end-effectors. However, these existing works focus on the mechatronics systems and mostly apply to dry brick stacking. The practical bricklaying process involves viscoelastic adhesives like mortar, critically affecting the strength of the constructed wall [17]. An accurate robotic bricklaying process with viscoelastic adhesives is essential to ensure construction quality in terms of both wall shape precision and structural strength.

Most works using the adhesives in the robotic bricklaying process apply a thin adhesive layer to the bricks, and position bricks according to a predetermined trajectory, ignoring the impact of maximum contact force on the consistency of brick bond strength. Note that mortar-jointed bricks' bond strength is influenced by the maximum contact force [18]. Semi-automated mason (SAM) [9] is a commercially available bricklaying robot that collaborates with workers to construct brick walls on-site with mortar. Pritschow et al. [1] developed a man-machine system involving a mobile bricklaying robot and a skilled worker utilizing thin-bed mortar. Dindorf et al. [10] presented an innovative solution for a mobile robotic unit equipped with a hydraulic lifting and leveling module, a brick warehouse, a brick belt feeder, and a mortar applicator. The Hadrian X [16] features a 30 m-long telescoping arm and a truck base for stacking concrete masonry units using polymer adhesive instead of traditional mortar according to a predefined plan. Shi et al. [8] proposed the anti-interference control strategy for the wall-building robot to ensure trajectory tracking accuracy with the uncertainty estimation in the robot dynamics model and the viscoelastic model of cement mortar. However, it is hard for existing works to guarantee the consistency of the bricklaying process due to the lack of force-position feedback control in the bricklaying process. To enhance the consistency of bond strength, the relationship between maximum contact force and bond strength is essential to be investigated. Thus, the force and position control are exploited to ensure the bricks are bonded with the desired position and maximum contact force.

The viscoelastic behavior of the mortar [19] poses challenges to position and force control in the bricklaying process. Leonhard et al. [18] proposed the integration of position and force control for the robotic bricklaying process, but this method cannot precisely reach the desired force and position. Rihani et al. [20] proposed the impedance control for the robotic brick masonry with the sacrificed position accuracy of bricks. Existing works on the force and position control in the bricklaying process are limited, but force and position control methods are widely explored in soft or unknown environments, including hybrid position/force control for soft tissue deformation modeling [21], force control with an active observer [22], force feedback control [23], neural network control [24], impedance control [25–28], and model predictive position/force control [29–31]. However, these existing methods are limited in the force and position control of the bricklaying process as they do not reach the desired maximum force while preserving position accuracy due to nonlinear viscoelastic mortar dynamics, and uncertain mortar thickness.

In this work, to address these issues, we propose the force-position control considering the nonlinear viscoelastic mortar dynamics to reach the desired position and maximum contact force in the robotic bricklaying process. The core contributions are summarized as follows:

- Identified the viscoelastic mortar dynamics and developed a feedforward bricklaying trajectory generation method to achieve the desired maximum contact force in the bricklaying process.
- Developed robotic bricklaying force-position feedback control method utilizing the mortar dynamics to ensure accurate final position and robust desired maximum contact force.
- Validated the feedforward and feedback controllers in robotic bricklaying experiments, as well as the relationship between the maximum contact force and the bricklaying bond strength with the standard shear test.

The detailed paper is structured as follows: Contact force-displacement mortar model and force reachability analysis are introduced in Section 2, followed by the feedforward trajectory generation method and robotic bricklaying force-position feedback control. Robotic bricklaying system modeling, including the identification of the robot dynamic model and contact force-displacement model of wet mortar, is detailed in Section 3. The robotic bricklaying experimental platform and validation of the proposed approach with simulation and experiments are detailed in Section 3, followed by case studies. Finally, the conclusion is illustrated in Section 4.

2. Force reachability analysis and dynamic robotic bricklaying force-position control design

This section analyzes the maximum contact force between bricks to determine the force reachability range. A feedforward bricklaying trajectory is designed to approach the desired maximum force within this range while ensuring placement accuracy. Additionally, a robotic bricklaying force-position feedback controller is introduced to ensure precise positioning and robust desired maximum contact force.

2.1. Contact force-displacement mortar dynamic model and force reachability analysis with multi-stage trapezoidal velocity approximation

The dynamic mechanical properties of the mortar are affected by some factors, such as the water-cement ratio R_w, sand-cement ratio R_s, temperature T, and curing time t_w. The normal contact force depends on the penetration p and contact velocity v for viscoelastic material. Based on the aforementioned factors, the contact force-displacement model of the bricklaying process over wet mortar is defined as

$$F = g(p, v, R_w, \mathrm{R}_s, T, t_w), \tag{1}$$

where $g(\cdot)$ represents the nonlinear function of the mortar force-displacement model. The cement utilized in this paper originates from the same batch, ensuring uniformity in its properties. To maintain the consistency of the experimental conditions, it is assumed that the water-cement ratio, sand-cement ratio, and mortar temperature are held constant throughout the experiment. Also, the curing process of the mortar is ignored, attributed to its rapid depletion during application. For simplification, Eq. (1) is rewritten as

$$F = g_s(p, v), \tag{2}$$

where $g_s(\cdot)$ represents the simplified nonlinear function of the mortar force-displacement model. Based on Eq. (2), the equation for the linearization of the mortar model $g_s(p,v)$ at the current state (p_c,v_c) is

$$\delta F=\frac{\partial g_s}{\partial p}|_{(p_c,v_c)}\delta p+\frac{\partial g_s}{\partial v}|_{(p_c,v_c)}\delta v=\frac{\partial g_s}{\partial p}|_{(p_c,v_c)}vdt+\frac{\partial g_s}{\partial v}|_{(p_c,v_c)}Adt, \tag{3}$$

where

$$\begin{aligned}\delta p&=p-p_c,\\ \delta v&=v-v_c,\end{aligned} \tag{4}$$

and A is the acceleration. According to the linearized model described in Eq. (3), $\widehat{F}_m$ is estimated with the penetration depth and contact velocity, defined as

$$\widehat{F}_m=\int_{t_0}^{t_e}\delta F=\int_{t_0}^{t_e}\frac{\partial g_s}{\partial p}vdt+\frac{\partial g_s}{\partial v}Adt. \tag{5}$$

Given $\widehat{F}_m$ defined in Eq. (5), the robot manipulator achieves different maximum contact forces by adjusting the velocity while preserving the desired position. Note that t_e is uncertain under different motion profiles while x_d is fixed, as shown in Fig. 1. The maximum contact force exerted between the bricks is constrained within a specific range due to the fixed mortar penetration depth and limited velocity. To investigate the range of the maximum contact force, the highest maximum contact force $\overline{F}$ is determined with the optimization, defined as

$$\begin{aligned}&\overline{F}=\max_{v(t)}\widehat{F}_m,\\ &\text{s.t. } x_d=x_0+\int_{t_0}^{t_e}vdt,\\ &0\le v(t)\le v_{\max},\\ &v(t_e)=0.\end{aligned} \tag{6}$$

The lowest maximum contact force $\underline{F}$ is obtained by solving a similar optimization problem. The maximum contact force reachability F_R is defined as

$$F_R\in[\underline{F}\ \ \overline{F}]. \tag{7}$$

F_R quantifies the achievable maximum contact force range within the specified constraints.

The velocity $v(t)$ along the compression trajectory and t_e are undetermined, as shown in Fig. 1 (b). To obtain F_R with the reduced computational load, the optimization variable $v(t)$ in Eq. (6) is approximated as the multi-stage trapezoidal velocity motion profile (solid line in Fig. 1 (b)). The robot manipulator accelerates or decelerates from the initial velocity v_0 to a specified velocity v_s with A_m^+ or A_m^- ($A_m^+=-A_m^-$), then moves at the constant velocity of v_s for Δt seconds and finally the velocity decelerates from v_s to 0 with A_m^- upon reaching x_d. Based on the multi-stage trapezoidal velocity motion profile, the position constraint in Eq. (6) is rewritten as follows

$$x_d=x_0+\int_{t_0}^{t_e}vdt=\begin{cases}x_0+\dfrac{v_s^2}{A_m^+}-\dfrac{v_0^2}{2A_m^+}+v_s\Delta t & \text{if } v_0\le v_s\\[2ex] x_0+\dfrac{v_0^2}{2A_m^+}+v_s\Delta t & \text{if } v_0>v_s\end{cases}. \tag{8}$$

With known x_0, x_d, v_0 and A_m^+ or A_m^- in the multi-stage trapezoidal velocity motion profile, $\widehat{F}_m$ is only influenced by v_s and Δt. $\widehat{F}_m$ in Eq. (5) is rewritten as

$$\widehat{F}_m=h_f(v_s,\Delta t)=h_f(v_s), \tag{9}$$

where Δt is represented by v_c based on Eq. (8) and $h_f(\cdot)$ is the function to decide the maximum contact force under the trapezoidal velocity motion profile, shown in Fig. 1 (b). $\overline{F}$ and $\underline{F}$ are given by

$$\begin{aligned}\overline{F}&=h_f(\overline{v}),\\ \underline{F}&=h_f(\underline{v}).\end{aligned} \tag{10}$$

2.2. Feedforward trajectory generation based on the mortar dynamics

To study the effect of the maximum contact force on bond strength, a general feedforward method based on mortar dynamics for robotic bricklaying systems is developed to reach different maximum contact forces. To reach F_d with the position and velocity constraints, the velocity $v(t)$ along the compressing trajectory is solved with the optimization problem Q with an unspecified terminal time, defined as

$$\begin{aligned}&Q=\min_{v(t)}\|\widehat{F}_m-F_d\|,\\ &\text{s.t. } x_d=x_0+\int_{t_0}^{t_e}vdt,\\ &0\le v(t)\le v_{\max},\\ &v(t_e)=0.\end{aligned} \tag{11}$$

To ensure F_d is achievable, F_d is set within the force reachability range F_R. To solve the optimization problem Q with the reduced computational load, the optimization variable $v(t)$ in Eq. (11) is approximated as the multi-stage trapezoidal velocity motion profile while maintaining the computing accuracy, as shown in Fig. 1. Despite the reduced computational complexity, the brick reliably reaches the predefined target position. Based on Eq. (8), the position constraint in Eq. (11) is converted to the function $h_x(\cdot)$ of two undetermined variables v_s and Δt. Accordingly, with the trapezoidal velocity motion profile, the optimization objective in Eq. (11) is converted to the function $h_f(\cdot)$ of v_s and Δt, given by

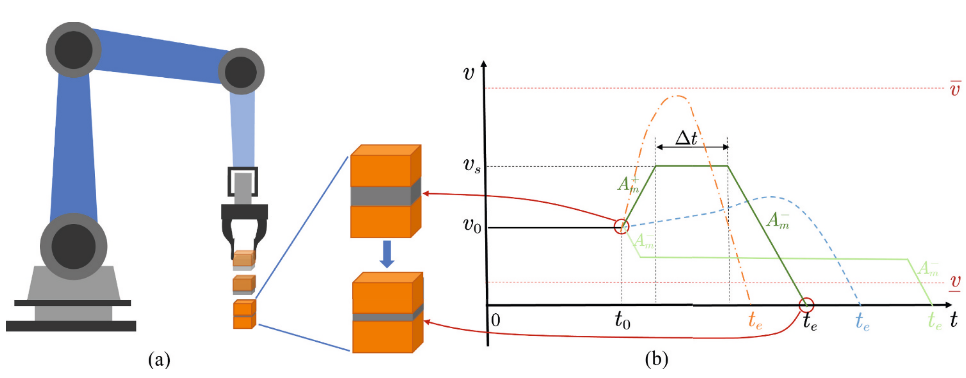

Fig. 1. (a) Robotic bricklaying process illustration, (b) Different motion profiles for different maximum contact forces with the uncertain end time t_e.

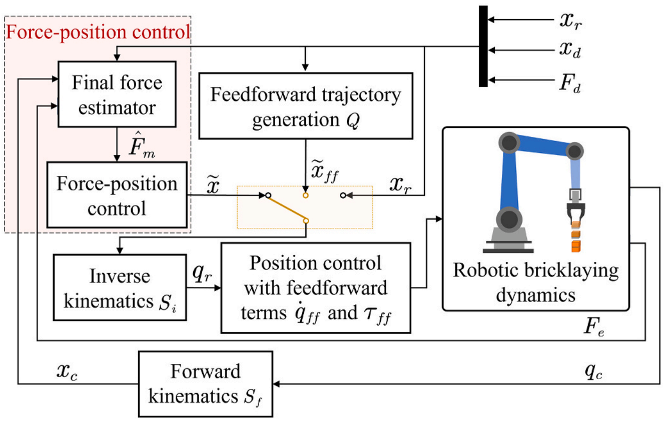

Fig. 2. Robotic bricklaying control diagram with the originally planned trajectory x_r, feedforward trajectory based on the mortar dynamics $\tilde{x}_{ff}$, and reshaped trajectory via force-position control $\tilde{x}$.

$$\begin{cases} x_d = x_0 + \int_{t_0}^{t_e} v dt = h_x(v_s \Delta t) \\ F_d = \hat{F}_m = \int_{t_0}^{t_e} \frac{\partial g_s}{\partial p} v dt + \frac{\partial g_s}{\partial v} A dt = h_f(v_s \Delta t) \end{cases}, \quad (12)$$
$$\text{s.t. } \underline{v} \le v_s \le \bar{v},$$
$$\Delta t \ge 0.$$

Using the binary Eq. (12), the motion profile is solved, determining the feedforward trajectory $\tilde{x}_{ff}$. The workflow is shown in Fig. 2.

2.3. Force-position feedback control design

The feedforward method relies on accurate mortar thickness and precise mortar dynamics, but in the application, uncertainties in the mortar thickness and mortar dynamics cause variations in the maximum contact force. To address this issue, this work proposes the general force-position control considering the mortar dynamics for robotic bricklaying systems, as shown in Fig. 2, to achieve the desired position and maximum contact force with the velocity constraint, defined as follows:

$$\begin{cases} \lim_{t \to t_e} (x(t)) = x_d \\ \max_{t \in (t_0, t_e)} (F_c(t)) = F_d \\ \lim_{t \to t_e} (v(t)) = 0 \end{cases}, \quad (13)$$

where $x(t)$ is the robot end effector position. The contact force F_c is given by

$$F_c = F_e - F_i. \quad (14)$$

The proposed force-position control method regulates velocity to achieve the desired maximum force during compression by relying on the real-time estimated maximum contact force based on the mortar dynamics, without changing the brick's target position. The control law for the velocity is

$$v_r = v_c + \delta v, \quad (15)$$

where δv is the velocity control increment. The velocity increment δv at each time step is

$$\delta v = A_n \delta t, \quad (16)$$

where

$$A_n = u(\hat{F}_m, F_d), \quad (17)$$

and $u(\cdot)$ is the function of $\hat{F}_m$ and F_d to regulate the acceleration. The velocity $v(t)$ along the compressing trajectory is unspecified and t_e is uncertain. For computational simplicity while maintaining the computing accuracy, the motion profiles (orange solid line) for the force-position control are established in Fig. 3 to estimate $\hat{F}_m$, with the robot manipulator either initially moving at a constant speed before decelerating to 0 at A_r^- (Case 1) or directly decelerating to 0 at A_0^- (Case 2, defined in Eq. (21)). Despite the parameterized motion profiles for reduced computation load, the brick consistently reaches the predefined target position. In Fig. 3, the green dashed line represents the originally planned trajectory, while the orange solid line shows the trajectory generated by the force-position control. From t_0 to t_c, the orange curve represents the reshaped trajectory based on force-position control. The straight section of the orange line from t_c to t_e the endpoint is the pre-planned trajectory for the remainder of the motion. The blue-shaded area, bounded by the orange trajectory, represents the region used to estimate $\hat{F}_m$ based on F_c. Given the settled motion profiles shown in Fig. 3, $\hat{F}_m$ is estimated in real time based on F_c and linearized mortar dynamics defined in Eq. (3), given by

$$\hat{F}_m = F_c + \int_{t_c}^{t_e} \delta F = F_c + \int_{t_c}^{t_e} \frac{\partial g_s}{\partial p} v dt + \frac{\partial g_s}{\partial v} A dt. \quad (18)$$

Define the gap distance Δx as

$$\Delta x = x_c - x_d. \quad (19)$$

Define the braking distance decelerating from v_c to 0 at A_r^- as x_b, given by

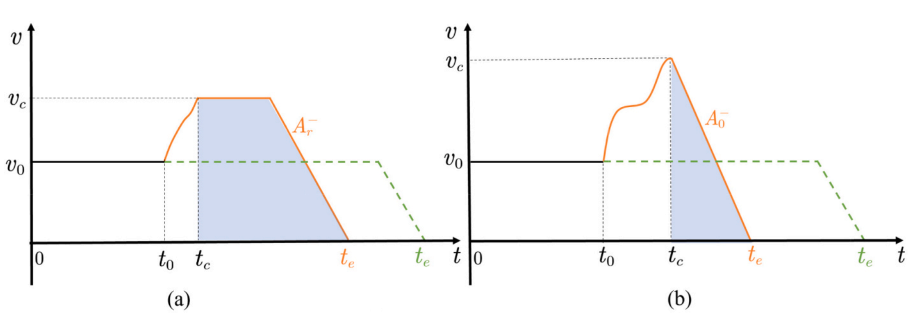

Fig. 3. Motion profiles for different cases of maximum contact force estimation. The green dashed line represents the originally planned trajectory, while the orange solid line shows the trajectory generated by the force-position control. The blue-shaded area, bounded by the orange trajectory, represents the region used to estimate $\hat{F}_m$. The two subplots illustrate different scenarios: (a) Case 1 of $x_b \le \Delta x$, (b) Case 2 of $x_b > \Delta x$. (For interpretation of the references to colour in this figure legend, the reader is referred to the web version of this article.)

Table 1
Pseudo algorithm of the acceleration regulation.

```
Input: current velocity v_c, current position x_c, current contact force F_c
Output: acceleration A_n
Main:
    Flag←1
    While Δx > 0 do
        If x_b ≤ Δx and flag> 0 then
            Motion profile←Case 1
            F̂_m based on Case
            A_n = A_r^- tanh((F̂_m − F_d)/k_f)
        else
            Flag←0
            Motion profile←Case 2
            F̂_m based on Case 2
            A_n = A_0^- + (A_m^- − A_0^-) tanh((F̂_m − F_d)/k_f)
        end
    end
    return A_n
```

$$x_b = -\frac{v_c^2}{2A_r^-} = \frac{v_c^2}{2A_r^+}, \tag{20}$$

where $A_r^+ = -A_r^-$. To avoid the overshooting from x_d, the comparison between Δx and x_b is conducted at each time step, as shown in Table 1. Define the deceleration A_0^- as

$$A_0^- = -\frac{v_c^2}{2\Delta x}. \tag{21}$$

The regulation of A_n for the velocity control increment δv is summarized in the pseudo algorithm shown in Table 1. With the updated v_r at each time step, the reshaped trajectory $\widetilde{x}$ is

$$\widetilde{x} = x_c + v_r\delta t. \tag{22}$$

3. Simulation and experiment verification

This section presents the hardware setup and identifies robot dynamics to minimize tracking errors and enhance dynamic response. Mortar dynamics are identified for simulations and experiments to validate the proposed feedforward and force-position feedback control methods. Finally, a case study on corner wall construction compares different methods, demonstrating the improved performance of the proposed force-position feedback control.

3.1. Hardware setup

To verify the proposed methods, the bricklaying robot is designed by combining a Huashu HSR-Co603 collaborative robot with a repeatability of 0.02 mm, a Hypersen HPS-FT060E load cell, and a ChangingTek CTAG2F120 gripper, as shown in Fig. 8 (a). The system's computational unit consists of an industrial computer equipped with an Intel i7–7700 CPU and 16 GB of RAM. The load cell, with a force resolution of 0.08 N and a moment resolution of 0.0015 Nm, is attached between the robot end effector and gripper. The robot joints, loadcell, and gripper are all controlled and sensed with the Beckhoff TwinCAT system via EtherCAT and RS485 communications with 1 kHz and 100 Hz sampling rates respectively, ensuring high real-time performance. The loadcell and connectors are characterized by rigidity, ensuring that the forces measured by the loadcell accurately correspond to the forces exerted at the contact brick. The force signals obtained from the loadcell are processed with zero calibration and the inertial force is subtracted.

3.2. Identification of robot dynamic model and tracking performance evaluation with torque and velocity feedforward

In the bricklaying contact process, the mortar is compressed with a short mortar penetration distance. The short penetration imposes significant challenges on the force-position control method because large tracking errors and the dynamic response of the robot manipulator affect the dynamic adjusting ability of force-position control. To address these challenges, feedforward terms based on the robot dynamic model [32] is exploited to mitigate the tracking error and improve the dynamic response of the robot manipulator. To identify the dynamic model of the bricklaying robot, the dynamic equation of a serial manipulator in the joint space is derived as

$$\tau_r = M(q)\ddot{q} + C(q,\dot{q})\dot{q} + g(q) + \tau_{\text{fric}}, \tag{23}$$

where $M(q)$ is the $n \times n$ inertia matrix, $C(q,\dot{q})$ is the n-vector containing Coriolis and centrifugal forces, $g(q)$ represents gravitational torques, and τ_{fric} is the n-vector friction force for an n-degree-of-freedom robot. The friction model for robot manipulators [33] is

$$\tau_{\text{fric}} = f_c \text{sign}(\dot{q}) + f_v \dot{q}, \tag{24}$$

where f_c and f_v are Coulomb and viscous friction coefficients respectively. Eq. (23) is linearized as

$$\tau_r = W_B(q,\dot{q},\ddot{q})P_B, \tag{25}$$

where W_B is a regression model only depending on the motion data, and P_B is a combination of the standard dynamic parameter set. To enhance the accuracy of identifying the dynamic parameter set P, the excitation trajectory is designed to fully stimulate the dynamic parameters specific to each axis of the robot. The excitation trajectory for each joint is a finite sum of K harmonic sine and cosine functions [33], given as

$$q_i(t) = q_{i0} + \sum_{l=1}^{K} \frac{a_l}{\omega_f l}\sin(\omega_f lt) - \frac{b_l}{\omega_f l}\cos(\omega_f lt), \tag{26}$$

where ω_f is the fundamental frequency, q_{i0} is the offset of the joint position of the excitation reference trajectories, and a_l and b_l are the amplitudes of the sine and cosine functions, determined through optimization. The feedforward terms are derived from the dynamic model of the bricklaying robot and external disturbances. By incorporating the feedforward terms, the final torque feedforward term τ_{ff} is given by

$$\tau_{ff} = \tau_r + J^\top F_e, \tag{27}$$

where J is the Jacobian matrix of the robot manipulator.

In this work, the excitation trajectories are designed with a five-term Fourier series of a fundamental frequency ω_f of 0.1 Hz. Optimization is based on the conditional number of W_B and kinematic constraints, resulting in an optimized excitation trajectory for the robot manipulator, as shown in Fig. 4. The Huashu robot executes the excitation trajectory, and the joint position, velocity, and torque are recorded via Beckhoff real-time control system. After low-pass filtering, the collected data is employed to fit the minimum dynamic parameter set P_B through the least squares method. The accuracy of the identified dynamic

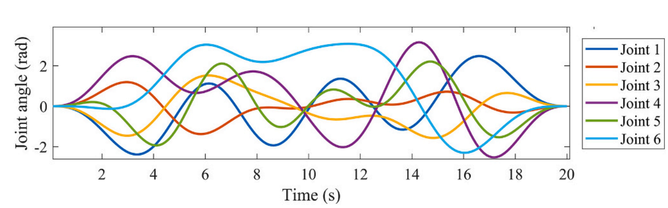

Fig. 4. Excitation trajectory.

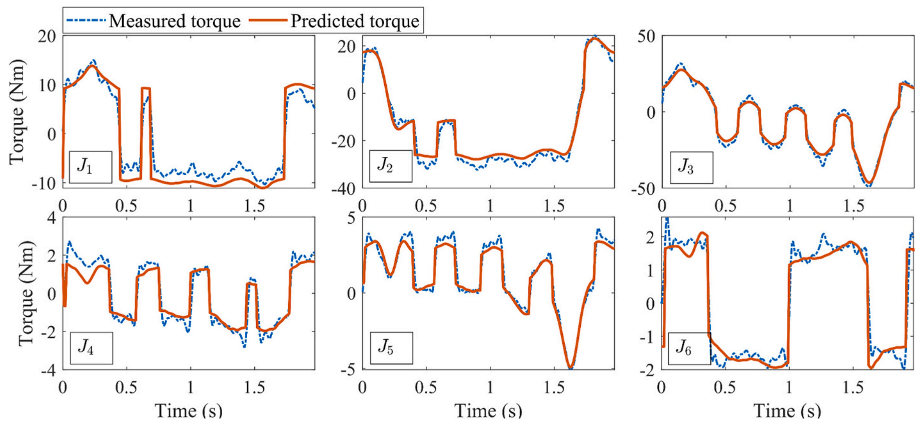

Fig. 5. Comparison between the measured and predicted torque with the identified minimum dynamic parameter set.

Table 2
Root mean square error between the measured and predicted torque with the identified minimum dynamic parameter set.

Joint	1st joint	2nd joint	3rd joint	4th joint	5th joint	6th joint
RSME (Nm)	2.6772	2.8364	2.7827	0.5486	0.4570	0.5061

parameters is validated by comparing the measured torque against the predicted torque using the parameter set P_B. This comparison, as shown in Fig. 5, demonstrates the validity of the identification results. Table 2 presents the root mean square error (RMSE) between the measured and predicted torque values. The first three joints exhibit larger RMSE values due to the higher driven torque requirements for these joints.

Effective force-position control in bricklaying requires precise tracking to respond quickly to the feedback force signal. The robotic bricklaying system utilizes a Proportional-Proportional-Integral (P-PI) position control structure. The system incorporates velocity feedforward $\dot{q}_{ff}$ and torque feedforward τ_{ff} into the P-PI position control framework to minimize tracking errors. Fig. 6 provides a comparative analysis of tracking errors with and without the feedforward terms. As the planned path is periodic, the tracking error shows periodic behavior. The increase in tracking error is observed during velocity reversals or at higher velocities. The results demonstrate a substantial reduction in both peak error generated during reversals and the steady-state error during constant velocity movement with the feedforward compensation.

3.3. Identification of force-displacement model of mortar

Due to the limited payload and workspace of the robot manipulator, uniformly sized acrylic bricks at a roughly 1:6 scale of standard Chinese red bricks, as specified by the Chinese national standard GB/T 5101–2017, are employed in this work. The proposed method is designed to be generalizable and applicable in actual construction settings. The physical properties of the mortar, such as its viscoelastic behavior, and bonding characteristic, remain the same regardless of the brick size. Thus, the use of scaled-down bricks effectively simulates the real-world bricklaying process. The manipulator initially grabs the brick and immerses it into the mortar. To ensure consistent mortar thickness, a scraper is employed to remove excess cement. The manipulator then presses the brick with mortar at different constant velocities, ranging from 1 mm/s to 5 mm/s in 1-mm/s increments. Each compression process at these velocities is repeated multiple times, with load cell measurements and position feedback recorded. Data collected during the deceleration phases are excluded from the analysis to maintain consistency. The average values of multiple sets of contact force and penetration depth data (indicated by the solid line in Fig. 7) are utilized to identify the mortar force-displacement model. The mortar dynamics in this paper are modeled based on experimental observations of its

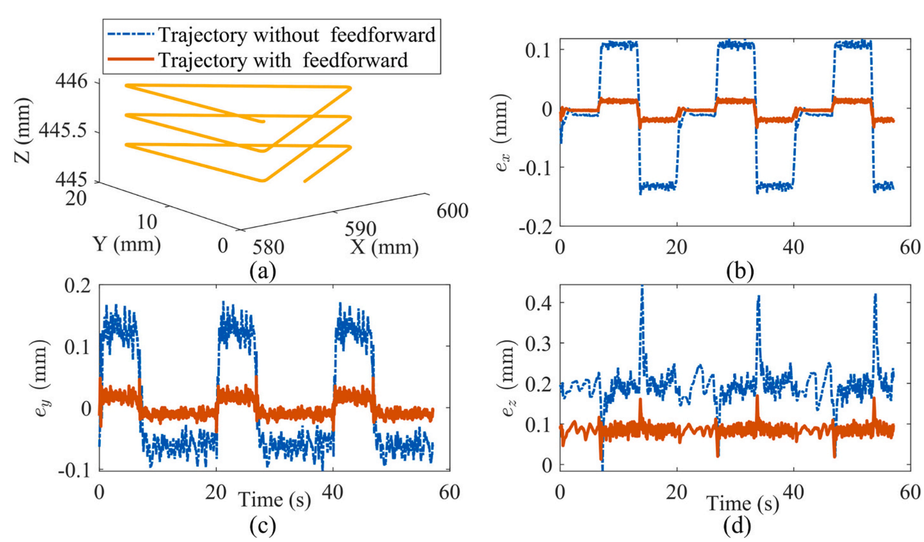

Fig. 6. (a) Planned trajectory for the tracking error comparison, (b-d) Tracking error comparison in X, Y, and Z direction between the position control with and without velocity and torque feedforward, showing reduced tracking error with feedforward compensation.

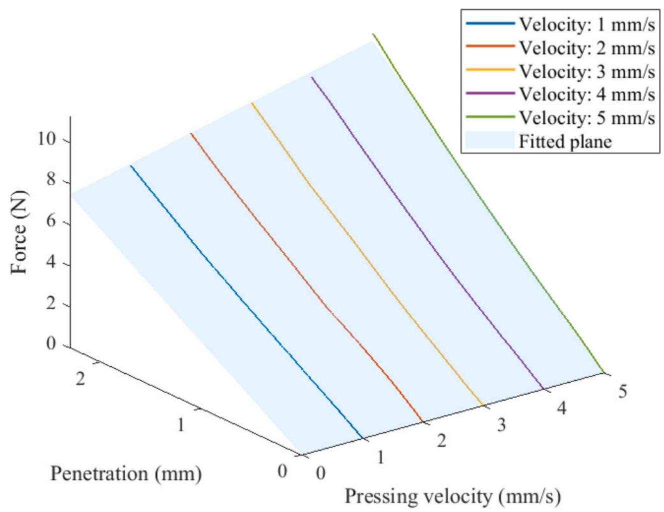

Fig. 7. Average value of multiple sets of contact force and penetration data under different velocities (solid line), and identified mortar force-displacement model based on force and penetration data under different velocities (blue plane). (For interpretation of the references to colour in this figure legend, the reader is referred to the web version of this article.)

viscoelastic behavior, consistent with the rheological characteristics studied in [34]. A theoretical linear relationship between torque and rotational speed in mortar flow is established and experimentally validated in [34]. This linearity aligns with our current mortar dynamics model, further supporting its reliability.

The least squares method is employed to fit the model, yielding the coefficient of determination R^2 of 99.51 %, as depicted in Fig. 7, indicating the desired fitting performance of the mortar force-displacement model. The mortar force-displacement model is

$$F = (av + b)p, \tag{28}$$

where a is 0.305 Ns/mm^2 and b is 3.25 N/mm. While the identified model predominantly captures the relationship between force, penetration, and velocity, model uncertainty still exists because the influence of the velocity change on the mortar force-displacement model is neglected in the identification process due to the inherent complexity of these interactions.

3.4. Simulation

This section presents the offline trajectory generation for robotic bricklaying. Simulations are conducted to validate the proposed feedforward and force-position feedback control methods.

3.4.1. Simulation of offline trajectory generation

The robotic bricklaying process is simulated offline, beginning with the robotic manipulator picking a brick from a designated basket. The brick is then immersed in mortar, with the excess mortar being scraped off to ensure even application before the brick is pressed onto a wall using force-position control. This process simplifies the process by eliminating the need for additional tools to spread the mortar on the bricks. During the dipping process, the brick is immersed sufficiently into the mortar to ensure sufficient mortar coverage for proper bonding between the bottom and sides of the bricks. To ensure accurate brick placement in the actual bricklaying process, a calibration procedure is performed to align the wall's coordinate system with that of the robot prior to the work scene establishment. After the entire wall is constructed, the robot uses a flat shovel to remove the excess mortar from the sides of the bricks, as shown in Fig. 8. Assuming a predefined working scenario, the path for the manipulator is generated using the Rapidly-Exploring Random Tree (RRT) algorithm [35]. Given the start position q_s and goal position q_g, the RRT algorithm expands by incrementally growing a random tree, and adding new nodes until the goal is reached while avoiding obstacles. This results in a path composed of line segments connected by nodes in the random tree. However, the inherent lack of smoothness in this path poses challenges for the manipulator's stable operation. To address this issue, the cubic spline function [36] is employed to interpolate between the points of the RRT-generated path, ensuring continuity and smoothness of the trajectory, Fig. 8(b) shows.

With the smooth trajectory obtained from the cubic spline function, time-optimal path planning [37] is exploited to generate the time-optimal trajectory. This trajectory specifies the position $q(t)$, velocity $\dot{q}(t)$, and acceleration $\ddot{q}(t)$, facilitating the precise movement of the manipulator along the path. The optimal time path planning is formulated as

$$\begin{aligned} &\min_{q(t)}\ T, \\ &\text{s.t. } |\dot{q}| < \dot{q}_m, \\ &\quad |\ddot{q}| < \ddot{q}_m, \end{aligned} \tag{29}$$

where T is the minimum arrival time under boundary velocity $\dot{q}_m$ and acceleration $\ddot{q}_m$ conditions.

3.4.2. Simulation of robotic bricklaying based on the identified mortar dynamics

According to the mortar force-displacement model in Eq. (28), the linearized mortar model is

$$\delta F = \underbrace{(av + b)\delta p}_{\frac{\partial g_s}{\partial p}\delta p}, \tag{30}$$

where the impact of δv on δF is ignored because the effect of velocity change on the mortar model is neglected in the model identification process. The initial velocity v_0 is set to 1 mm/s, $\underline{v}$ is set to 0.2 mm/s, and $\overline{v}$ is set to 8 mm/s. Given the fixed physical distance between the designed trajectory and the scraper, the mortar thickness l is estimated at approximately 2.3 mm, based on the gap between the bottom surface of the brick and the scraper. A gap between two bricks l_g is set to 0.5 mm. A_m^+ is set to 100 mm/s^2. Based on Eqs. (5) and (30), $\widehat{F}_m$ is given by

$$\widehat{F}_m = \int_{t_0}^{t_e} \delta F = \int_{t_0}^{t_e} (av + b)\delta p = \int_{t_0}^{t_e} (av + b)v dt. \tag{31}$$

According to the motion profile introduced in Fig. 1 and Eq. (10), the lowest and highest maximum contact forces between bricks are 5.96 N and 9.73 N, respectively. With determined $\underline{F}$ and $\overline{F}$, the maximum contact force range is set to 6–9 N with a 1-N sampling step for the feedforward method and force-position control. Based on the aforementioned parameters, the feedforward trajectory is solved via the constraint Eq. (12) with various desired maximum contact forces from 6 N to 9 N (1-N sampling step). Fig. 10 reveals that the final contact force grows as velocity increases and the desired position and maximum contact force are achieved.

To verify the proposed force-position control of the bricklaying process, a simulation based on the identified mortar dynamics is established. The simulation workflow is depicted in Fig. 2. During the force-position control, $\widehat{F}_m$ is estimated at each time step based on Eqs. (18) and (30) with the designed motion profile shown in Fig. 3, given by

$$\widehat{F}_m = F_c + \int_{t_c}^{t_e} \delta F = F_c + \int_{t_c}^{t_e} (av + b)\delta p = F_c + \int_{t_c}^{t_e} (av + b)v dt. \tag{32}$$

In the force-position feedback control simulation, additional parameters include A_r^+ of 80 mm/s^2 and k_f of 1 N. The force-position

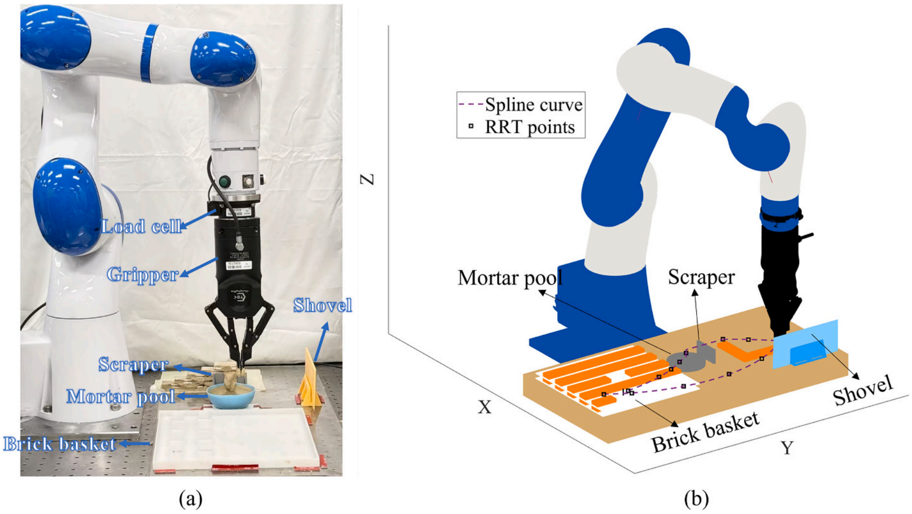

Fig. 8. (a) Bricklaying robot hardware setup, (b) Offline robotic bricklaying trajectory generation with RRT path planning, and spline curve smoothing.

control is activated when the contact force surpasses 0.5 N. Due to the variance in mortar thickness, the simulation is conducted under different mortar thicknesses to achieve the same desired position and maximum contact force, as shown in Fig. 9 (a). The method successfully achieves a consistent desired maximum contact force of 8 N despite varying mortar thicknesses l from 2.3 to 2.7 mm, while reaching the desired position. As the mortar thickness increases, the downward motion slows down to maintain the same maximum contact force.

To validate the proposed algorithm's ability to adjust to different maximum contact forces, the simulation is conducted under the same mortar thickness to achieve the same desired position and different maximum contact forces, and the simulation result is shown in Fig. 9 (b). Both the desired position and different maximum contact forces are reached. As the maximum contact force increases, the downward motion speeds up to ensure the target force is reached. These two above simulations demonstrate the proposed method's ability to maintain consistent maximum contact forces despite variations in mortar thickness and adapt different maximum contact forces despite the same mortar thickness while reaching the desired position. The proposed force-position control method can adjust the maximum contact force between bricks within a reachable range. The primary goal is not to maximize the contact force for each brick but to achieve a consistent maximum contact force across all bricks, thereby improving the uniformity of the bricklaying process.

3.5. Experimental validation of the robotic bricklaying process with different methods and bond strength comparison under different maximum contact forces

The bricklaying robot joins two bricks with a 0.5-mm gap using a pressing velocity of 1 mm/s. Under this case, the mean value of multiple sets of maximum contact forces is 8.1333 N, with a standard deviation of 1.4946 N, influenced by the uncertainty in mortar thickness. According to the feedforward method simulation, the feedforward trajectories are executed by the robot manipulator to explore the relationship between maximum contact force and bond strength. Experimental results in Fig. 10 reveal that the final contact force grows as velocity increases. The theoretical contact force does not exactly match the actual force due to the uncertainty of mortar thickness and mortar model.

The feedforward method cannot reach precisely the preset maximum contact force. Thus, bricklaying force-position feedback control based on the viscoelastic mortar dynamics is proposed to achieve the desired maximum contact force and position. In the experiment, some parameters are set as follows: A_m^+ of 20 mm/s^2, A_r^+ of 10 mm/s^2, and k_f of 2 N.

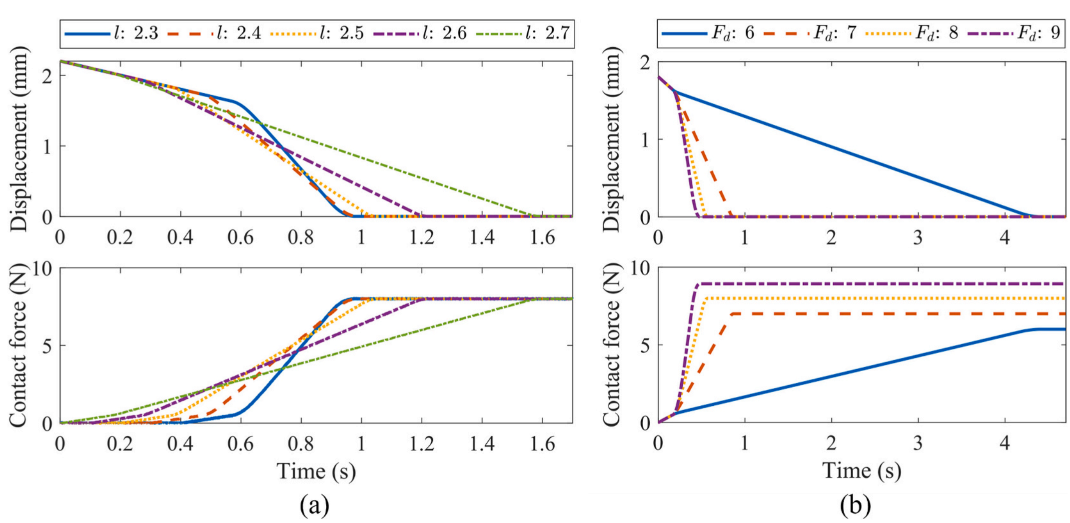

Fig. 9. (a) Simulation of force-position control with the same desired position and maximum contact force 8 N under different mortar thicknesses from 2.3 to 2.7 mm, (b) Simulation of force-position control with the same desired position and different desired forces from 6 N to 9 N under the same mortar thickness 2.3 mm.

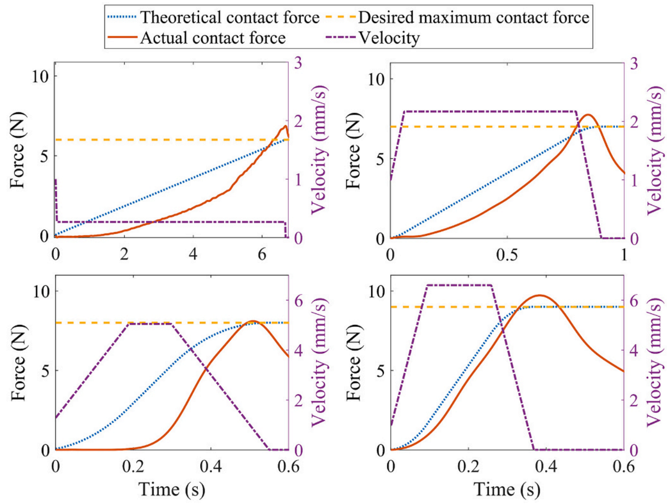

Fig. 10. Representative contact forces of the feedforward method and feedforward trajectories with different velocities based on the mortar dynamics under the desired maximum contact force of 6, 7, 8, and 9 N.

The proposed force-position control method reaches the desired maximum contact force, as shown in Fig. 11. The blue line represents the estimated maximum contact force, and the actual force gradually converges the desired maximum contact force meanwhile the estimated maximum contact force progressively aligns with and eventually coincides with the actual contact force.

Both feedforward and force-position feedback control methods exhibit position errors less than 0.05 mm, within the robot's repeatability range shown in Fig. 12. The standard deviation in the maximum contact force of the feedforward method under multiple sets of experiments is roughly equivalent to that of constant velocity compressing of 1 mm/s. The variation in the maximum contact force of the feedforward method is notable due to the uncertainty of mortar thickness and mortar dynamics, as shown in Fig. 13. The standard deviation of the desired maximum force for force-position feedback control is notably lower than that of the feedforward approach, as detailed in Table 3. The force-position control achieves the desired position and force with reduced variation, enabling further exploration of the relationship between maximum contact force and bond strength and the consistency of the bricklaying process.

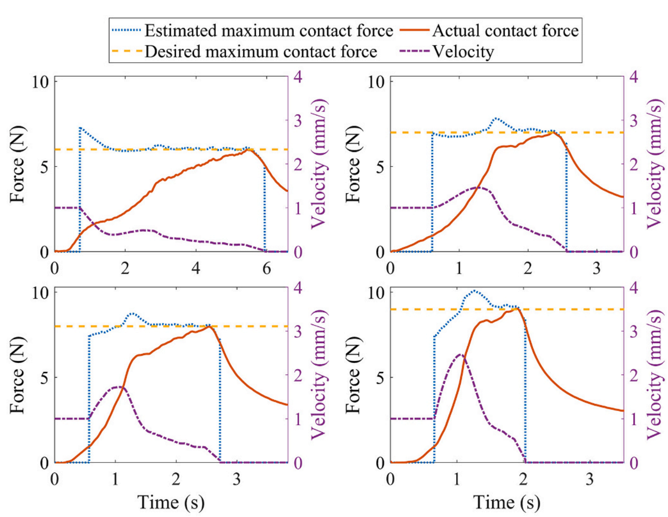

Fig. 11. Experimental contact force and the corresponding velocity of the force-position feedback control under the desired maximum contact force of 6, 7, 8, and 9 N in the robotic bricklaying process.

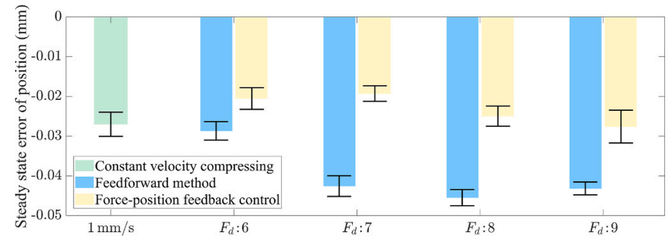

Fig. 12. Steady-state error of final position of multiple sets of experiments under constant velocity compressing of 1 mm/s, and different desired maximum contact forces F_d with the feedforward method and the force-position feedback control.

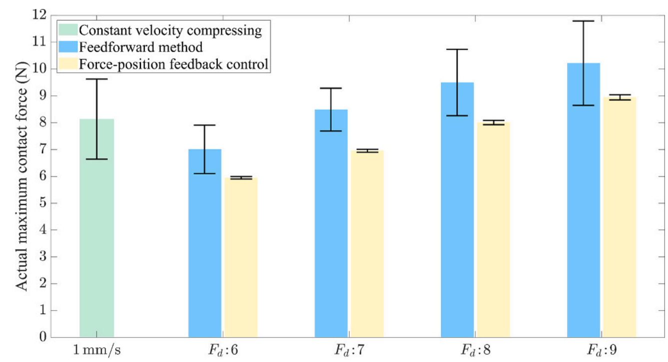

Fig. 13. Actual maximum compressing force of multiple sets of experiments under constant velocity compressing of 1 mm/s, and different desired maximum contact forces F_d with the feedforward method and the force-position feedback control.

Table 3
Analysis of the actual and desired maximum contact force.

Desired maximum contact force (N)		6	7	8	9
Relative error of actual and desired maximum contact force	Feedforward method	16.83 %	21.24 %	18.72 %	13.53 %
	Feedback control	0.88 %	0.62 %	0.09 %	0.63 %
Standard deviation of actual maximum contact force (N)	Feedforward method	0.9016	0.7965	1.2362	1.6739
	Feedback control	0.0483	0.0588	0.0817	0.0958

To compare the energy consumption across different methods, the instantaneous power P at each time step was calculated with

$$P = \sum_{i=1}^{6} U_i I_i, \quad I_i = \tau_{fi} / K_{\tau i}, \tag{33}$$

where I_i is the motor current, derived from the torque feedback τ_{fi} and the motor's torque constant $K_{\tau i}$, and U_i is the voltage. The average power across different methods ranges from 30.1693 W to 33.9217 W, as the robot moves downward from 2.5 mm above the target brick placement. The mean value of the average power for all methods is 32.4611 W with a standard deviation of 0.9727 W, indicating consistent power usage across methods.

Shear bond strength serves as the main metric for the bond strength in brick walls according to EN 1052–3 [38], exploited to reveal the relationship between maximum contact force and bond strength. To do the shear test on the bonded bricks, the electromechanical test system

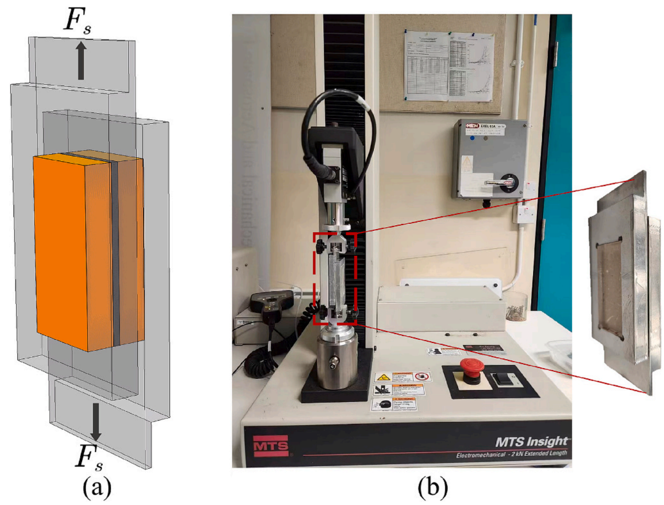

Fig. 14. (a) Shear test illustration for the bonded bricks (black: cement, orange: bricks, semi-transparent: clamping components), (b) Shear test hardware setup.

with a force capacity of 2000 N from Mechanical Testing & Simulation Company is employed, as shown in Fig. 14. Shear bond strength τ_s is defined as [39]

$$\tau_s = F_s/A_c, \tag{34}$$

where F_s is the maximum shear force when the bonded bricks break, and A_c is the contact area between two bricks of masonry.

The paper investigated the shear bond strength of multiple sets of bonded bricks pressed at a velocity of 1 mm/s, revealing a mean shear bond strength of 0.124 MPa with a standard deviation of 1.66×10^{-2}MPa. To investigate the relationship between the bond strength and maximum contact force, shear tests on the bonded bricks are conducted to demonstrate the difference in the shear strength under different maximum contact forces. Shear test results indicate a positive correlation between shear bonding strength and maximum contact force, regardless of the method employed (feedforward or force-position feedback control), as illustrated in Fig. 15. Compared with the feedforward method, the variation in shear bond strength of the constant velocity compressing is roughly equivalent. Compared with the force-position control, the variation in shear bond strength of the feedforward method is notable due to the large variation of the maximum contact force in the feedforward method. The results in Table 4 reveal that force-position feedback control exhibits reduced variation in shear strength compared with the feedforward method and enhanced shear bond strength compared with constant velocity pressing, promising a consistent quality of robotic bricklaying products.

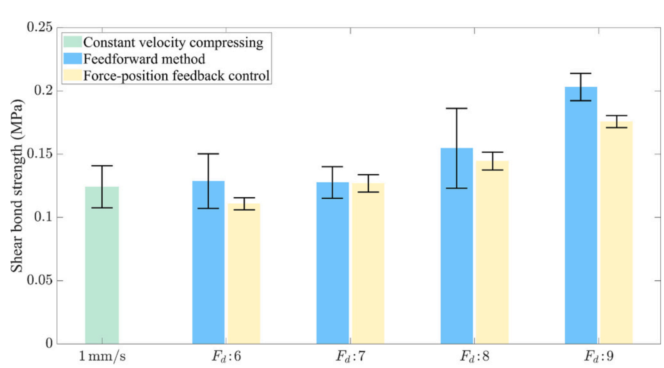

Fig. 15. Shear bond strength of multiple sets of experiments under constant velocity compressing of 1 mm/s, and different desired maximum contact forces F_d with the feedforward method and the force-position feedback control.

Table 4
Standard deviation of the shear bond strength under different maximum contact forces.

Standard deviation of shear bond strength under different maximum contact forces	6 N	7 N	8 N	9 N
Feedforward method (MPa)	2.16×10^{-2}	1.25×10^{-2}	3.16×10^{-2}	1.08×10^{-2}
Feedback control (MPa)	4.80×10^{-3}	6.84×10^{-3}	7.02×10^{-3}	4.72×10^{-3}

3.6. *Case study of corner wall built with robotic bricklaying force-position control*

To implement the proposed method in the robotic bricklaying work, a corner brick wall is designed and constructed, as shown in Fig. 16 (a) and (b). In this case study, the corner brick walls are built with constant velocity compressing of 1 mm/s, feedforward trajectory generation, and force-position feedback control. To ensure the consistent quality and high bond strength of brick walls, the desired maximum contact force between bricks is set to 9 N for the feedforward and feedback method, as determined in Section 3.5. The bonding quality is assessed visually, particularly in the horizontal and vertical joints between the bricks. The use of transparent acrylic bricks and base allows for clear observation of the mortar filling between the bricks, ensuring that the mortar fills the joints and forms adequate bond marks at the bottom surface of the bricks. Additionally, the bricks are detached after bonding to verify that the filling of both horizontal and vertical joints is sufficient. The built corner wall is further evaluated based on wall shape accuracy and the maximum contact force between bricks.

The accuracy of the external surface geometry of the constructed brick wall is measured using an EinScan Pro HD optical 3D scanner. To obtain the precise shape of the built corner brick wall, a robotic shovel is first used to roughly remove excess mortar. A small amount of residual mortar is then removed manually to prevent interference with the comparison between the actual wall shape and the theoretical design. The scanning process captures the entire 3D model of the brick wall, facilitated by a rotation stage to ensure comprehensive coverage. The scanned 3D model of the brick wall is matched and compared with the theoretical model using Geomagic Control X. The resulting wall shape error maps under three methods are depicted in Fig. 17. The detailed shape error of built corner walls, including the maximum deviation and RMSE, is analyzed in Table 5. The shape errors of the corner wall under different methods are similar, underscoring the robustness of the system in achieving the desired bricklaying positions, regardless of the specific method used. The bricklaying robot utilizes an absolute positioning system, helping to alleviate the accumulated position errors. These

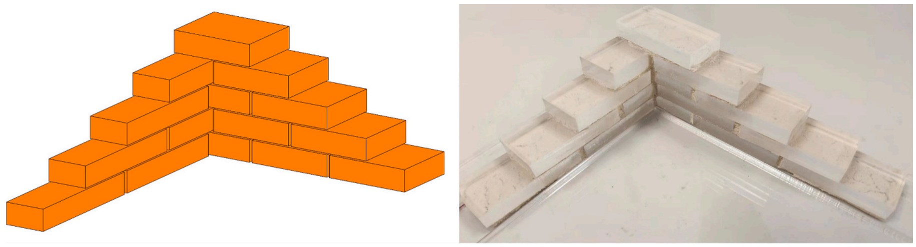

Fig. 16. (a) Theoretical corner wall model, (b) Built corner brick wall.

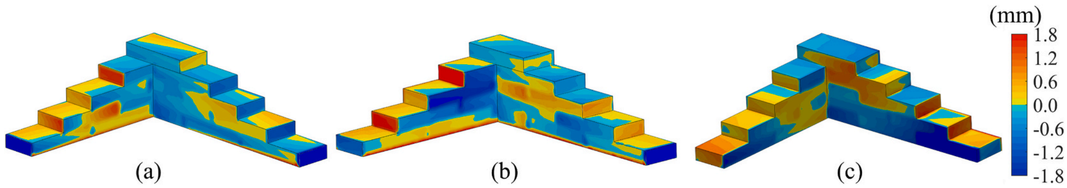

Fig. 17. Shape error maps of the corner wall under (a) constant velocity compressing, (b) feedforward trajectory generation, and (c) force-position control.

Table 5
Analysis of the shape error of built corner walls under constant velocity compressing, feedforward trajectory generation, and force-position control methods.

Wall building methods	Constant velocity compressing	Feedforward trajectory generation	Force-position control
Maximum deviation	1.8275 mm	1.8793 mm	1.7582 mm
RMSE	0.9643 mm	0.9471 mm	0.9539 mm

errors originate from several factors, including small misalignments in the arrangement of bricks within the brick basket, slight inaccuracies in brick shape, and minor interferences during the gripping motion.

The maximum contact force of each brick under the three methods is illustrated in Fig. 18. The experiment results show that the feedforward trajectory generation method increases the maximum contact force compared with the constant velocity compressing. The variation of the maximum contact force is larger in the constant velocity compressing and feedforward trajectory generation compared with the force-position control. In the robotic bricklaying process, the manipulator immerses the bricks into the mortar and subsequently scrapes off the excess mortar. However, this procedure results in mortar layers that are unintentionally thicker or thinner than anticipated. The large variation of the maximum contact force in the constant velocity compressing and feedforward trajectory generation is attributed to inconsistencies in mortar thickness. Table 5 and Table 6 demonstrate that the proposed force-position control method reaches the desired maximum contact force with small variations while building the wall accurately, enhancing the consistency of the bricklaying process.

Table 6
Analysis of the maximum contact force of each brick in the built corner walls under constant velocity compressing, feedforward trajectory generation, and force-position control methods.

Wall building methods	Constant velocity compressing	Feedforward trajectory generation	Force-position control
Mean value of the maximum contact force	7.8483 N	9.7495 N	8.9027 N
Standard deviation of the maximum contact force	1.6155 N	1.7080 N	0.3190 N

4. Conclusion

This paper established a control-based method to enhance the robotic bricklaying process consistency. The control framework was decomposed into feedforward and feedback approaches. The feedforward control converted the optimal bricklaying trajectory generation problem to an optimal control problem with unspecified terminal time. The optimal control problem, considering the viscoelastic mortar dynamics, was parameterized with multi-stage trapezoidal velocity to reduce the computational complexity. On top of the feedforward trajectory, a force-position feedback control method was proposed to achieve consistent maximum contact force and accuracy, despite the process uncertainty. The feedback control method dynamically estimated the maximum contact force based on the real-time force feedback signals; it further planned the velocity profiles to ensure that the brick's final position and contact forces were desirable. The proposed methods have been validated with various simulation and experiment case

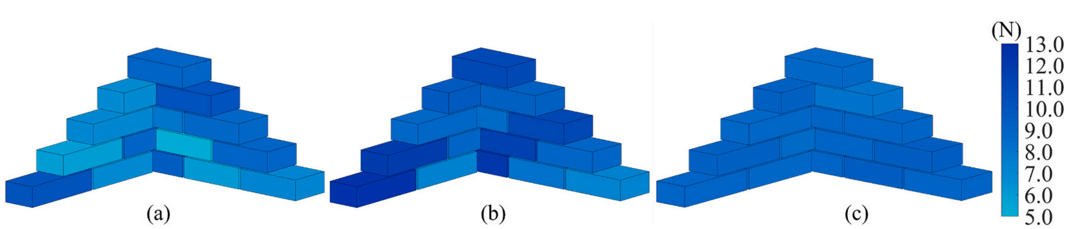

Fig. 18. Maximum contact force maps of the corner wall under (a) constant velocity compressing, (b) feedforward trajectory generation, and (c) force-position control.

studies. In simulations, the proposed force-position control was verified with two cases: consistent maximum contact force despite variations in mortar thickness and different maximum contact forces under the same mortar thickness. In experiments, the robot manipulator equipped with the load cell and gripper pressed the brick to the desirable position and maximum contact force robustly despite the bricklaying process uncertainty. Shear tests on the bonded bricks demonstrated that the proposed method achieved bond strength with reduced variation. Thus, the proposed force-position control method showed enhanced consistency in the robotic bricklaying process. Future studies aim to adapt the proposed method to more complex masonry structures and irregular bricks. Advanced tools like laser systems will be integrated to enhance absolute positioning accuracy and refine calibration between the robotic bricklaying system and the constructed wall. Additionally, expanding the robot's operational range by incorporating mobile platforms or dual-arm configurations, automating plastering for direct mortar application on the brick bottom and side efficiently, and integrating force-position control for both the bricklaying and wall surface plastering processes, will be explored.

Supplementary data to this article can be found online at https://doi.org/10.1016/j.autcon.2025.106090.

Declaration of Generative AI and AI-assisted technologies in the writing process

During the preparation of this work the authors used ChatGPT and Grammarly AI in order to perform grammar checks. After using this tool/service, the authors reviewed and edited the content as needed and take full responsibility for the content of the publication.

CRediT authorship contribution statement

Yi Zhou: Writing – review & editing, Writing – original draft, Visualization, Validation, Software, Methodology, Investigation, Formal analysis, Data curation. **Bowen Huang:** Visualization, Validation, Data curation. **Boge Dong:** Visualization, Validation, Data curation. **Yi Wen:** Software, Data curation. **Molong Duan:** Writing – review & editing, Writing – original draft, Supervision, Project administration, Methodology, Investigation, Funding acquisition, Conceptualization.

Declaration of competing interest

The authors declare that they have no known competing financial interests or personal relationships that could have appeared to influence the work reported in this paper.

Acknowledgment

The authors acknowledge support from the Research Grants Council (RGC) of the Government of Hong Kong Special Administrative Region (HKSAR) with RGC/ECS Project (No. 26215824), the Frontier Technology Research for Joint Institutes with industry scheme under grant OKT24EG07, as well as the HKUST – HKUST(GZ) Cross-campus Collaborative Research Scheme under the Great Bay Area "1 + 1 + 1" Joint Funding Program. This work was supported in part by the Project of Hetao Shenzhen-Hong Kong Science and Technology Innovation Cooperation Zone (HZQB-KCZYB-2020083). The help from the funding agency and the other researchers is sincerely appreciated.

Data availability

Data will be made available on request.

References

[1] G. Pritschow, M. Dalacker, J. Kurz, M. Gaenssle, Technological aspects in the development of a mobile bricklaying robot, Autom. Constr. 5 (1996) 3–13, https://doi.org/10.1016/0926-5805(95)00015-1.
[2] Y. Zhou, M. Duan, Vibration compensation of an extendable variable-stiffness boom-lift-mounted robot, IEEE/ASME Trans. Mechatron. (2024) 1–9, https://doi.org/10.1109/TMECH.2024.3402054.
[3] A.V. Malakhov, D.V. Shutin, K.V. Marfin, Ways of improving performance of mobile bricklaying robotic systems, J. Phys. Conf. Ser. 1679 (2020) 8–12, https://doi.org/10.1088/1742-6596/1679/5/052004.
[4] M. Gharbia, A. Chang-Richards, Y. Lu, R.Y. Zhong, H. Li, Robotic technologies for on-site building construction: a systematic review, J. Build. Eng. 32 (2020) 101584, https://doi.org/10.1016/j.jobe.2020.101584.
[5] Y. Liu, H. Jebelli, Human-Robot Co-Adaptation in Construction: Bio-Signal Based Control of Bricklaying Robots, Computing in Civil Engineering 2021 - Selected Papers from the ASCE International Conference on Computing in Civil Engineering 2021, 2021, pp. 304–312, https://doi.org/10.1061/9780784483893.038.
[6] M. Rakovic, M. Jovanovic, B. Borovac, B. Tepavčević, M. Nikolić, M. Papovic, Design and fabrication with industrial robot as brick-laying tool and with custom script utilization, in: 23rd International Conference on Robotics in Alpe-Adria-Danube Region, IEEE RAAD 2014 - Conference Proceedings, 2015, p. 4, https://doi.org/10.1109/RAAD.2014.7002251.
[7] V. Usmanov, M. Bruzl, S. Pavel, R. Šulc, Modelling of industrial robotic brick system, in: ISARC 2017 - Proceedings of the 34th International Symposium on Automation and Robotics in Construction, 2017, pp. 1013–1021, https://doi.org/10.22260/isarc2017/0140.
[8] Q. Shi, Z. Wang, Z. Zheng, Z. Zhou, Z. Wang, Y. Guo, P. Wu, Trajectory tracking control of a wall-building robot in an uncertain viscoelastic environment, Autom. Constr. 166 (2024) 105611, https://doi.org/10.1016/j.autcon.2024.105611.
[9] Construction Robotics, SAM. https://www.construction-robotics.com/sam-2/, 2024.
[10] R. Dindorf, P. Woś, Innovative solution of mobile robotic unit for bricklaying automation, J. Civil Eng. Transp. 4 (2022) 21–32, https://doi.org/10.24136/tren.2022.014.
[11] K. Dörfler, T. Sandy, M. Giftthaler, F. Gramazio, Mobile robotic brickwork, robotic fabrication in architecture, Art Design (2016) 204–217, https://doi.org/10.1007/978-3-319-26378-6_15.
[12] V. Helm, S. Ercan, F. Gramazio, M. Kohler, Mobile robotic fabrication on construction sites: DimRob, in: IEEE International Conference on Intelligent Robots and Systems, 2012, pp. 4335–4341, https://doi.org/10.1109/IROS.2012.6385617.
[13] Y. Wu, H.H. Cheng, A. Fingrut, K. Crolla, Y. Yam, D. Lau, CU-brick cable-driven robot for automated construction of complex brick structures: from simulation to hardware realisation, in: 2018 IEEE International Conference on Simulation, Modeling, and Programming for Autonomous Robots 2018, SIMPAR, 2018, pp. 166–173, https://doi.org/10.1109/SIMPAR.2018.8376287.
[14] M. Ambrosino, P. Delens, E. Garone, Control of a multirobot bricklaying system, in: Advanced Control for Applications: Engineering and Industrial Systems 3, 2021, pp. 1–19, https://doi.org/10.1002/adc2.90.
[15] L. Piškorec, D. Jenny, S. Parascho, H. Mayer, F. Gramazio, M. Kohler, The brick labyrinth, robotic fabrication in architecture, Art Design (2019) 489–500, https://doi.org/10.1007/978-3-319-92294-2.
[16] FastBrick Robotics, Hadrian X. https://www.fbr.com.au/view/hadrian-x, 2023.
[17] A.T. Vermeltfoort, Brick-mortar Interaction in Masonry under Compression, PhD thesis, 2005, https://doi.org/10.6100/IR589402.
[18] B.L.E. Bernold, F.R. Altobelli, H. Taylor, Computer-Controlled Brick Masonry 6, 1992, pp. 147–160, https://doi.org/10.1061/(ASCE)0887-3801(1992)6:2(147).
[19] R. Bouras, C. Si Hadj Mohand, M. Sonebi, Adhesion and rheology of joints fresh mortars, J. Mater. Eng. Struct. 6 (2019) 157–165. https://revue.ummto.dz/index.php/JMES/article/view/1774.
[20] R.A. Rihani, L.E. Bernold, Methods of control for robotic brick masonry, Autom. Constr. 4 (1996) 281–292, https://doi.org/10.1016/0926-5805(95)00009-7.
[21] G. Duchemin, P. Maillet, P. Poignet, E. Dombre, F. Pierrot, A hybrid position/force control approach for identification of deformation models of skin and underlying tissues, IEEE Trans. Biomed. Eng. 52 (2005) 160–170, https://doi.org/10.1109/TBME.2004.840505.
[22] P. Moreira, N. Zemiti, C. Liu, P. Poignet, Viscoelastic model based force control for soft tissue interaction and its application in physiological motion compensation, Comput. Methods Prog. Biomed. 116 (2014) 52–67, https://doi.org/10.1016/j.cmpb.2014.01.017.
[23] Y. Yang, Y. Zhou, M. Duan, Contact-force-based closed-loop control of shell structure additive manufacturing with continuous-fiber-reinforced polymer composites, J. Mater. Proces. Tech. 331 (2024) 118501, https://doi.org/10.1016/j.jmatprotec.2024.118501.
[24] S. Bhasin, K. Dupree, P.M. Patre, W.E. Dixon, Neural network control of a robot interacting with an uncertain viscoelastic environment, IEEE Trans. Control Syst. Technol. 19 (2011) 947–955, https://doi.org/10.1109/TCST.2010.2054094.
[25] J. Duan, Y. Gan, M. Chen, X. Dai, Adaptive variable impedance control for dynamic contact force tracking in uncertain environment, Robot. Auton. Syst. 102 (2018) 54–65, https://doi.org/10.1016/j.robot.2018.01.009.
[26] X. Chen, R. Wang, Q. Ren, Variable force tracking control via online learning, in: Proceedings of the 18th IEEE Conference on Industrial Electronics and Applications 2023, ICIEA, 2023, pp. 215–220, https://doi.org/10.1109/ICIEA58696.2023.10241937.
[27] M. Hajimiri, H.A. Talebi, M. Zareinejad, Force tracking impedance control of robot-tissue interaction with a hunt-crosseley model, in: 2016 4th International

Conference on Control, Instrumentation, and Automation 2016, ICCIA, 2016, pp. 142–147, https://doi.org/10.1109/ICCIAutom.2016.7483151.

[28] Z. Feng, W. Liang, J. Ling, X. Xiao, K.K. Tan, T.H. Lee, Adaptive robust impedance control for an ear surgical device with soft interaction, in: IEEE/ASME Transactions on Mechatronics 27, 2022, pp. 1784–1795, https://doi.org/10.1109/TMECH.2021.3087014.

[29] J. De La Casa Cardenas, A.S. Garcia, S.S. Martinez, J.G. Garcia, J.G. Ortega, Model predictive position/force control of an anthropomorphic robotic arm, in: Proceedings of the IEEE International Conference on Industrial Technology 2015-June, 2015, pp. 326–331, https://doi.org/10.1109/ICIT.2015.7125119.

[30] C.H. Chou, M. Duan, C.E. Okwudire, A linear hybrid model for enhanced servo error pre-compensation of feed drives with unmodeled nonlinear dynamics, CIRP Ann. 70 (2021) 301–304, https://doi.org/10.1016/j.cirp.2021.04.070.

[31] C.-H. Chou, M. Duan, C.E. Okwudire, A physics-guided data-driven feedforward tracking controller for systems with unmodeled dynamics – applied to 3D printing, IEEE Access (2023), https://doi.org/10.1109/ACCESS.2023.3244194.

[32] X. Shao, S. Wang, L. Yang, N. Liu, Research on feedforward control based on robot dynamics parameters identification, in: 2020 IEEE International Conference on Mechatronics and Automation, ICMA 2020, 2020, pp. 973–978, https://doi.org/10.1109/ICMA49215.2020.9233788.

[33] J. Swevers, W. Verdonck, J. De Schutter, Dynamic model identification for industrial robots, IEEE Control. Syst. Mag. 27 (2007) 58–71, https://doi.org/10.1109/MCS.2007.904659.

[34] P.F.G. Banfill, Rheological methods for assessing the flow properties of mortar and related materials, Constr. Build. Mater. 8 (1994) 43–50, https://doi.org/10.1016/0950-0618(94)90007-8.

[35] C. Ma, Y. Zhang, Q. Zhao, K.F. Bai, 6R serial manipulator space path planning based on RRT, in: Proceedings - 2016 8th International Conference on Intelligent Human-Machine Systems and Cybernetics, IHMSC 2016 2, 2016, pp. 99–102, https://doi.org/10.1109/IHMSC.2016.90.

[36] E.T.Y. Lee, Choosing nodes in parametric curve interpolation, Comput. Aided Des. 21 (1989) 363–370, https://doi.org/10.1016/0010-4485(89)90003-1.

[37] H. Pham, Q.C. Pham, A new approach to time-optimal path parameterization based on reachability analysis, IEEE Trans. Robot. 34 (2018) 645–659, https://doi.org/10.1109/TRO.2018.2819195.

[38] EN 1052–-3, Methods of Test for Masonry–Part 3: Determination of Initial Shear Strength, 2007. ISBN: 9780580603556.

[39] K. Javed, M.I. Ul Hassan, M.A. Farooq, M.B. Sharif, Detailed investigation of compressive and bond strength for sustainable brick masonry developed by using various types of bricks and green mortars, J. Build. Eng. 84 (2024) 108477, https://doi.org/10.1016/j.jobe.2024.108477.